

²³Na Solid-State NMR Analyses for Na-Ion Batteries and Materials

Kazuma Gotoh^{*[a, b]}

Sodium-ion batteries (NIBs) have received considerable attention as next-generation batteries that complement or replace the current demand for lithium-ion batteries. For the development of NIBs, elucidating the states of sodium ions and understanding the charging-discharging mechanism on the electrodes is indispensable for achieving high capacity, high efficiency, long life, and reasonably safe performance. Solid-state nuclear magnetic resonance (SS-NMR) is a powerful tool for obtaining direct information on nuclei as it can detect

information on sodium and distinguish different electronic circumstances. In this minireview, recent progress on NMR analyses of NIB electrode materials (cathode and anode) is outlined. ²³Na NMR signals of NaMnO₂-type cathodes, which are usually affected by the strong effect of paramagnetic species and other cathode materials, are introduced. Additionally, NMR analyses of hard carbon, graphite, and other inorganic anode materials are summarized.

1. Introduction

Sodium-ion batteries (NIBs) are receiving considerable attention as next-generation batteries that complement or replace the demand for current lithium-ion batteries (LIBs) for use in portable devices (PC and smart phones), electric vehicles (EVs), and stationary power supplies. Abundant resources of sodium, Cu/Co-free configuration, and the similar standard electrode potential of Na compared to Li, are advantageous to next-generation batteries. Some NIB components, such as binders and separators are common with LIBs; however, NIBs do not work only by replacing the lithium compounds with sodium compounds in the electrode materials. Therefore, every NIB material, such as the active materials in the electrodes (cathode and anode) and electrolyte solutions, requires research for practical use in NIBs.^[1]

For the development of NIBs with higher capacity, higher efficiency, longer lifetime, and acceptable safety, elucidating the states of the sodium ions and the mechanism of charging-discharging on the electrodes is indispensable. In many analyses of batteries and battery materials, solid-state nuclear magnetic resonance (SS-NMR) is a powerful tool for obtaining direct information of nondestructive elements (nuclei). As NMR can obtain information on sodium or lithium nuclei and can distinguish different electronic circumstances by measuring ²³Na, ⁷Li, or ⁶Li, it is suitable for the analysis of complicated

systems consisting of many components and elements, such as NIBs and LIBs. In particular, the NMR properties that can be used to analyze the electronic properties of Li or Na in both crystal compounds and amorphous materials are greatly advantageous because several intermediate phases of cathode and anode materials often exhibit amorphous structures that cannot be analyzed by X-ray diffraction (XRD). Hard carbon (HC), which is the most promising anode material for practical use, also has a non-crystalline structure.

For the NMR analysis of LIBs, ⁷Li and ⁶Li measurements are performed. ⁷Li is mainly observed owing to its stronger sensitivity (signal intensity) and higher gyromagnetic ratio, while ⁶Li is sometimes applied because of the narrower (sharp) signals in the spectra owing to the smaller quadrupole moment (Table 1). Conversely, ²³Na is a unique stable isotope of sodium. The sensitivity of ²³Na is relatively high in NMR active nuclei, but lower than that of ⁷Li, making ²³Na NMR analysis easy (Table 1). The spin-lattice relaxation time (T_1) of ²³Na NMR is usually very short (<0.1 s), which also facilitates analysis using Na NMR.

The chemical shifts and peak shapes (width and structure) of signals in the NMR spectra are dependent on several interactions. Although local diamagnetic shielding by electrons has a dominant influence on the chemical shift of the common

[a] Dr. K. Gotoh
Graduate School of Natural Science & Technology
Okayama University
3-1-1 Tsubshima-naka, Okayama 700-8530, Japan
E-mail: kgotoh@okayama-u.ac.jp

[b] Dr. K. Gotoh
Element Strategy Initiative for Catalysts and Batteries (ESICB)
Kyoto University
Nishikyo-ku, Kyoto 615-8245, Japan
An invited contribution to a joint Special Collection between ChemElectroChem and Batteries & Supercaps dedicated to research Beyond Lithium-Ion Batteries

Table 1. Parameters of ¹H, ²H, ⁶Li, ⁷Li, ²³Na, ³¹P, and ⁵¹V nuclei.

Isotope	Spin	Natural abundance [%]	Quadrupole moment [10^{-28} m^2]	Sensitivity (relative)	NMR frequency [MHz] at a field of 11.744 T
¹ H	1/2	99.98	–	1.00	500.00
² H	1	1.5×10^{-2}	2.73×10^{-3}	9.65×10^{-3}	76.75
⁶ Li	1	7.42	-8.0×10^{-4}	8.50×10^{-3}	73.58
⁷ Li	3/2	92.58	-4.5×10^{-2}	0.29	194.32
²³ Na	3/2	100	0.12	9.25×10^{-2}	132.26
³¹ P	1/2	100	–	6.63×10^{-2}	202.40
⁵¹ V	7/2	99.76	-5.2×10^{-2}	0.38	131.45

nuclei of solution NMR, such as ^1H and ^{13}C , the shielding effect is relatively small compared to the other major interactions in the case of Li and Na NMR ($\pm 20 \sim 30$ ppm, in most cases for Na measurements). The paramagnetic effect caused by paramagnetic species, such as metals in cathode materials (Mn, Ni, etc.) largely influences Na peaks. The effect usually broadens the signal owing to the very short spin-spin relaxation time (T_2) and shifts the peak to a higher frequency. For example, the Na ion affected by paramagnetic Mn^{4+} showed a peak at 1000–1800 ppm (vs. diamagnetic NaCl_{aq} at 0 ppm) in ^{23}Na NMR. By contrast, the Knight shift, which is caused by the susceptibility produced by conduction electrons in conductive materials, is significant in anode materials, such as carbon and metal electrodes. The shifts of ^7Li metal and ^{23}Na metal signals are observed at approximately 263 and 1130 ppm, respectively (vs. LiCl_{aq} and NaCl_{aq} at 0 ppm). By contrast, quasi-metallic states of Li and Na (observed in almost fully lithiated and sodiated HC electrodes, respectively) exhibit signals between the metal shifts and 0 ppm, depending on their metallic character (i.e., the cluster size of the Li and Na). However, in the case of alloy compounds, the signals of Na nuclei in crystalline Na_xM_y (M : metal atom in anode) show peak shifts depending on their electronic circumstances in the crystal. The peaks can be ascribed to Na sites in the compounds using a combination of NMR, XRD, and first-principle calculations. Furthermore, the effect of bulk magnetic susceptibility should also be considered in direct *in situ* or *operando* NMR measurements of "cell" samples. The spectra of cells consisting of electrode plates and current collector plates are strongly affected by this susceptibility effect, which induces large shifts of Na peaks depending on the angle between the electrode plates in the cell and the direction of the static magnetic field (B_0), particularly for paramagnetic samples.

In this minireview, recent progress for Na NMR analyses of NIB electrode materials (cathode and anode) is summarized. As it is impossible to describe all studies using NMR measurements in this review, studies primarily using NMR to investigate the state of electrodes were chosen. In terms of cathode materials, 2D layered manganese oxide compounds (Na_xMnO_2) and partially substituted compounds of Na_xMnO_2 , which have been most frequently analyzed using NMR, are primarily discussed. Some NMR studies of the other cathode compounds are also covered. In terms of anode materials, ^{23}Na NMR analyses of HC and alloy compounds (Sb, Sn, and P) are mainly discussed. Molecular dynamics analyses of Na-complexes in graphite

anodes using ^1H and ^{2}H NMR and research on two-dimensional nanosheet anodes are also mentioned.

2. Cathode (Positive Electrode) Materials

Several sodium transition metal oxide compounds have been reported as suitable cathode materials for NIBs. Most of these are ternary or quaternary systems, consisting of mainly 3d transition metal elements (e.g., Mn, V, and Fe) with a small content of additive hetero atoms. Some of these materials are paramagnetic, which broadens the width of ^{23}Na NMR signals and shifts the peak position (chemical shift) of the peaks. The chemical shifts of some materials are higher than those of the Na metal signal (1130 ppm) because of the strong effect of the paramagnetic species. Particularly, the paramagnetism of Mn largely increases or decreases depending on the valence state and distribution of electron density around the Mn atoms, which is useful in distinguishing the transitions of the electronic state of Na using the Na NMR spectra.

As a larger magnetic field is a disadvantage to the NMR of strong paramagnetic samples, NMR using a lower magnetic field (4.7–7.0 T) is preferred for measuring cathode materials. High-speed magic-angle spinning (MAS; 30–120 kHz) is useful for narrowing broad signals and distinguishing peaks above each component in the cathode materials.

2.1. Mn Compound Materials

Several Na_xMO_2 ($0 < x \leq 1$, M: a transition metal such as Fe, Cr, Ni, or Mn) compounds with a 2D layered structure have been reported as cathode materials with superior properties.^[2] These materials can replace the use of costly cobalt in the cathode with abundant and inexpensive resources. One such material, NaMnO_2 , is a layered compound showing polymorphism, wherein the redox-active metal atom is Mn. Among the polytypes of NaMnO_2 and its derivatives, $\beta\text{-NaMnO}_2$, and some compounds with Mn atoms being partly substituted for other metals (e.g., Mg or Ni, $\text{Na}_{2/3}\text{Mn}_{1-y}\text{Mg}_y\text{O}_2$ ($y \leq 0.1$) or $\text{Na}_x\text{Ni}_{x/2}\text{Mn}_{1-x/2}\text{O}_2$ ($x \leq 0.3$)) have been reported. In these compounds, the Mn^{3+} ion forms an MnO_6 octahedron, and the Na ions are intercalated between the layers consisting of MnO_6 octahedra. $\beta\text{-NaMnO}_2$ exhibits a high capacity (ca. 190 mAh g^{-1} at a rate of 0.05 C) and good capacity retention (100 mAh g^{-1} after 100 cycles at 2 C). It also contains a small (2%) intergrown region of



Kazuma Gotoh is currently an Associate Professor of the Department of Chemistry, Faculty of Science, at Okayama University, Japan. He received his Ph.D. degree from Tsukuba University in 2002. His research focuses on NMR analyses of nanostructured inorganic materials, such as carbon materials, and electrochemical energy storage devices (i.e., lithium-ion and sodium-ion batteries).

α -NaMnO₂ structure, as revealed by XRD and ²³Na NMR. In β -NaMnO₂ compounds, a major peak in the Na NMR signal was observed at 237 ppm. Minor peaks also appear at 650 and 433 ppm, which are ascribed to the signal of α -NaMnO₂ and the signal of Na in the vicinity of a planar defect (twin boundary), respectively.^[3] The intensities of these peaks decrease with electrochemical desodiation, and new peaks broadened by the strong paramagnetism of Mn⁴⁺ form and grow up. The signal of Na in Na_{0.51}MnO₂ was observed at approximately 700 ppm. As shown in Figure 1, the peak shifted to 1000 ppm for the composition between Na_{0.51}MnO₂ and Na_{0.28}MnO₂.

Some compounds with Mn atoms partly substituted for other metals, such as Mg or Ni, resulting in Na_{2/3}Mn_{1-y}Mg_yO₂ ($y \leq 0.1$) or Na_xNi_{x/2}Mn_{1-x/2}O₂ ($x \leq 0.3$), respectively, have also been analyzed using ²³Na NMR. Mg substitution improves the rate performance and capacity retention of the electrode. The 5% Mg-doped phase exhibits a superior rate performance for cathodes with a P2 (ABBA stacking of oxygen layers) structure, with a reversible capacity of 106 mAh g⁻¹ at a very high discharge rate of 5000 mA g⁻¹. The reduction in the number of Jahn-Teller distorted Mn³⁺ ions disrupts the potential of the Mn³⁺/Mn⁴⁺ ordering, which leads to fewer structural and electronic processes occurring during battery cycling.^[4] The ²³Na NMR data provides direct evidence of fewer oxygen layer shearing events, leading to a stabilized P2 phase structure and an enhanced Na-ion mobility of up to 3.8 V vs. Na⁺/Na upon Mg doping. The Na signals of the compound shifted from 650–1150 ppm (Na sites with Mn³⁺ being predominant) to 1450–1800 ppm (Na sites with Mn⁴⁺ being predominant) based on

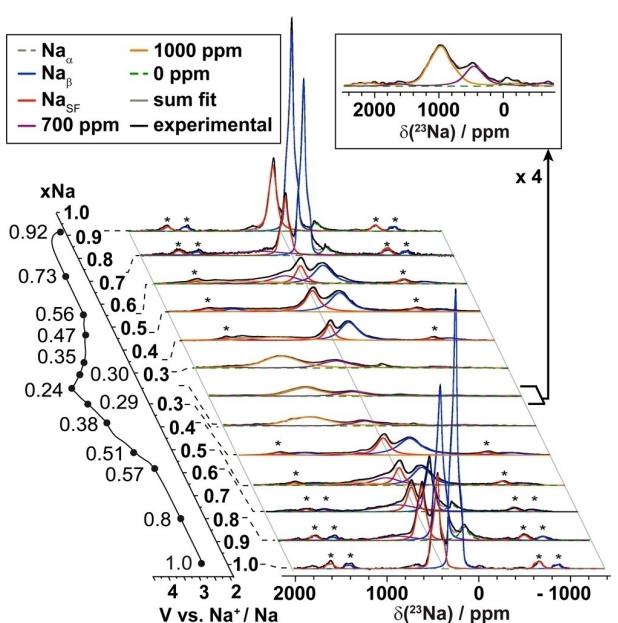


Figure 1. ²³Na MAS NMR spectra of P2–Na_xMnO₂. A major peak of Na_β (β -NaMnO₂ like environment (blue component)), and two minor peaks of Na_α (α -NaMnO₂ like environment (green component)) as well as Na_{SF}(Na in the vicinity of a twin boundary(red component)) are observed in $x \geq 0.9$ compounds. New peaks broadened by the strong paramagnetism of Mn⁴⁺ appear for $x \leq 0.4$. Reprinted from Ref. [3b] with permission. Copyright (2016) American Chemical Society.

the change in the layer structures and the composition of the compounds^[4] (Figure 2). A large shift of the Na signal to a higher frequency is also observed in the K-modified P2–Na_{0.7}Mn_{0.8}Mg_{0.9}O₂.^[5] The presence of K perturbs the local environment of Na and exhibits broader signals in the NMR spectra.

In Ni-doped compounds, ²³Na NMR can be used to indirectly observe the oxidation of Ni ions. There are three reported layer stacking structures, P2 and P3 (ABBCCA), and O3 (ABCABC), for the Na_xNi_{x/2}Mn_{1-x/2}O₂ compounds (Figure 3). The ²³Na NMR spectra of each compound showed peaks at approximately 1450, 1280, and 1700 ppm for P2, P3, and O3 stacking, respectively.^[6] The P2 compound (Na_{0.78}Ni_{0.23}Mn_{0.69}O₂)

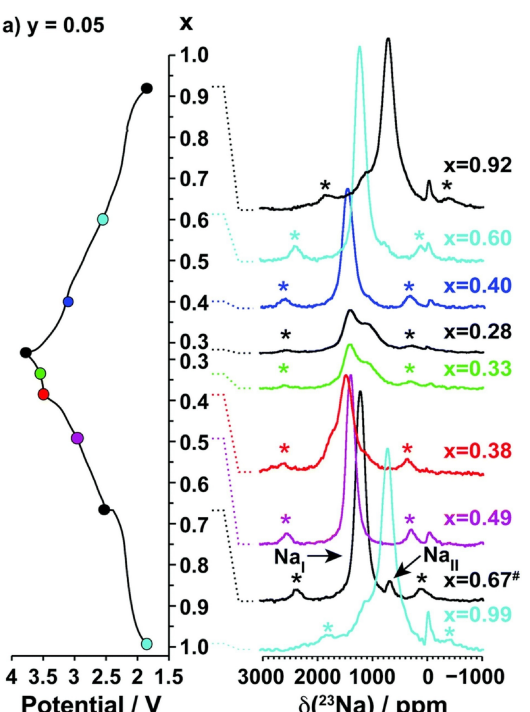


Figure 2. ²³Na MAS NMR spectra of Na_xMn_{1-y}Mg_yO₂ ($y = 0.05$) and the electrochemical curve. The Na signals of the compound shift from lower frequency shift (Na sites with Mn³⁺ being predominant) to higher frequency shift (Na sites with Mn⁴⁺ being predominant). Reproduced from Ref. [4] under the terms of the Creative Commons License. Copyright (2016) Royal Society of Chemistry.

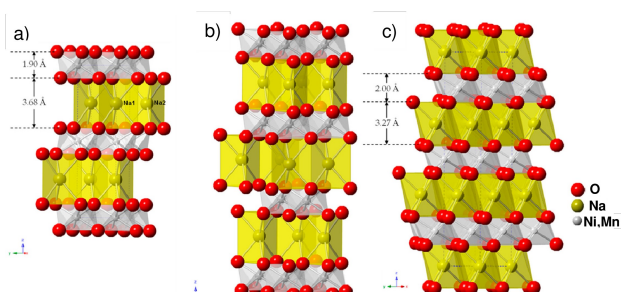


Figure 3. Three different layer stacking structures of Na_xNi_{x/2}Mn_{1-x/2}O₂ compounds, a) P2, b) P3, and c) O3. Reprinted from Ref. [6] with permission. Copyright (2013) American Chemical Society.

shows a reversible capacity of 138 mAh g⁻¹ at an average electric potential of 3.25 V (vs. Na⁺/Na) with a single smooth voltage profile even with changes to O₂ stacking over 4.2 V; thus, the compound is used by maintaining the potential under 4.1 V^[7] or adding small amounts of Li to stabilize the material.^[8] The pristine sample of Na_{0.78}Ni_{0.23}Mn_{0.69}O₂ shows a major ²³Na NMR peak at 1423 ppm (Figure 4). The peak shifts reversibly between 1423 and 984 ppm, depending on the state of charge

(SOC), which is the inverse of the shift of P2-Na_xMnO₂ and Na_{2/3}Mn_{1-y}Mg_yO₂ (Figures 1 and 2). The shift is explained by the oxidation of Ni from Ni²⁺ to Ni⁴⁺, rather than the oxidation or reduction of Mn. *Ab initio* calculations supported the model of rapid exchange of Na in P2 layers.

²³Na NMR can also be used to observe hydration, the effect of vacancies in the transition metal layers, and the substitution effect of transition metals of the cathode compounds. In the case of P2-Na_{2/3}Mn_{0.8}Fe_{0.1}Ti_{0.1}O₂, wherein a part of Mn is substituted with Fe and Ti, a major peak of ²³Na appears at 1230 ppm, and shifts with the change in Ti(IV) content.^[9] Hydrate compounds with H₂O or D₂O show a new broad signal at 303 ppm (Figure 5).^[9a] The broad signal with a reduced paramagnetic shift is attributed to the subtly increasing interlayer space in combination with a modified local environment induced by the hydroxyl grouping in the interlayer space. An increased Na-O-M distance significantly reduces the amount of unpaired electron density delocalized from the metal to the sodium site. In another report, Al- and Fe-containing Na_xMnO₂ (Na_{0.6}Al_{0.1}Fe_{0.05}Mn_{0.85}O₂), with a high initial capacity of 202 mAh g⁻¹ within 2–4 V, was investigated using XRD and Na NMR.^[10] Rapid quenching of the material induces the formation of vacancies in transition metal layers and enhances the Mn⁴⁺/Mn³⁺ redox centers. Consequently, the deliverable capacity of the material can be significantly improved because of the elimination of the factors that cause capacity decay. ²³Na NMR clearly shows the slight difference in Na sites and distortion of the P2 structure. The effects of K-, Rb-, and Cs-modification on the state of Na in P2-Na_{0.7}Mn_{0.8}Mg_{0.2}O₂,^[11] substitution effects of Na_{2/3}Mn_{0.2}M_{0.1}M'_{0.1}O₂ (M, M'=Fe³⁺, Al³⁺, Zn²⁺, Cu²⁺, Ti⁴⁺),^[12] and the Li-stabilized compound (Na_{0.8}Li_{0.2}Fe_{0.2}Mn_{0.6}O₂)^[13] have also been reported recently.

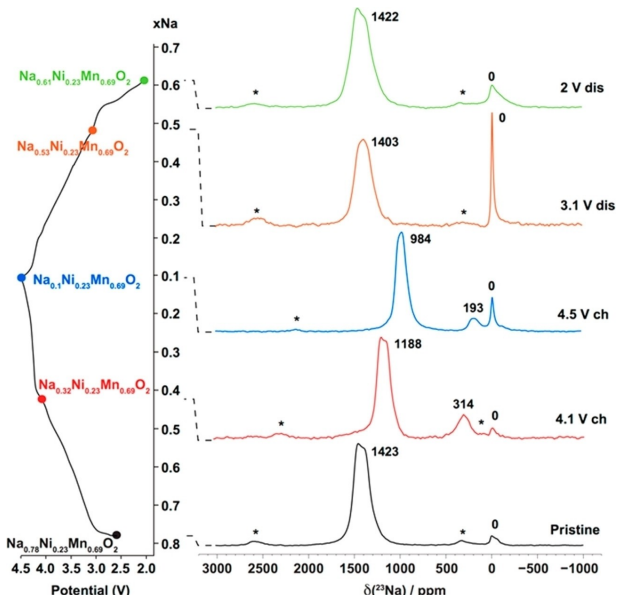


Figure 4. ²³Na MAS NMR spectra of Na_{0.78}Ni_{0.23}Mn_{0.69}O₂ and the electrochemical curve. Reprinted from Ref. [7] with permission. Copyright (2017) American Chemical Society.

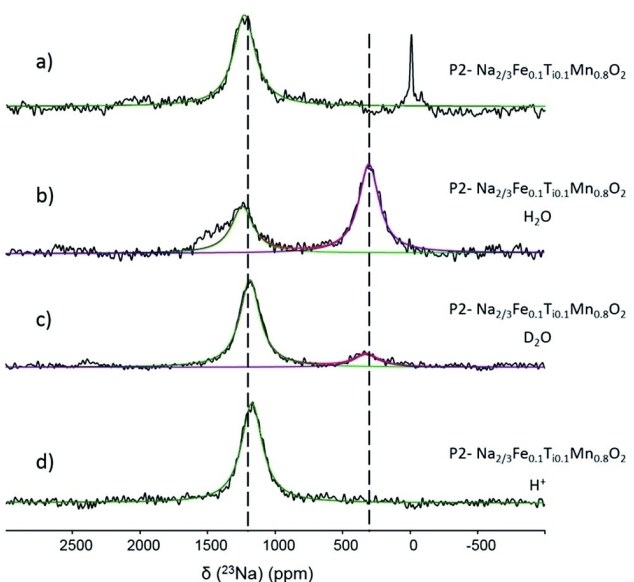


Figure 5. a) ²³Na NMR spectra of Na_{2/3}Mn_{0.8}Fe_{0.1}Ti_{0.1}O₂, b) hydrated (H₂O) phase, c) hydrated (D₂O) phase, and d) protonated phase. The peaks observed at 1230 and 303 ppm are assigned to Na⁺ under the paramagnetic effect caused by transition metal and Na⁺ coordinated to the OH group inside the sodium layers of the material, respectively. Reproduced from Ref. [9a] with permission. Copyright (2016) Royal Society of Chemistry.

2.2. Other Cathode Materials

Several cathode materials, apart from Mn compounds, have also been suggested, and NMR is an important tool for the structural analysis of these materials. Na₃V₂(PO₄)₂O_xF_{3-x} ($0 \leq x \leq 2$)^[14] compounds are fluorine-based polyanionic compounds with superior charge-discharge properties, which were investigated using ²³Na NMR (*ex situ* and *in situ*) and ³¹P *ex situ* NMR. It has been reported that two ²³Na NMR peaks attributed to the different Na sites at 89–92 and 128–146 ppm^[15] come together by changing the F content in the compound,^[16] or shifting to a lower frequency based on charging.^[17] ⁵¹V NMR analyses were also performed to confirm the formation of V(V)^[18] and state of V(III) and V(IV).^[19] The state of V in another compound, NaVOPO₄, containing V(III), V(IV), and V(V), was also analyzed using ²³Na, ³¹P, and ⁵¹V NMR.^[20] Na₂FePO₄F, a compound similar to Na₃V₂(PO₄)₂O_xF_{3-x}, was also analyzed using ²³Na NMR^[21] and ²³Na exchange spectroscopy (EXSY) NMR.^[22] The ²³Na EXSY NMR revealed a slow exchange between the two Na sites. In iron-doped compounds, such as Na₃V_{2-y}O_{2-y}Fe_y(PO₄)₂F_{1+y}, the degree of vanadium substitution has been estimated using NMR and magnetic susceptibility measurements.^[23]

3. Anode (Negative Electrode) Materials

3.1. Hard Carbon

Carbon materials can be used as negative electrodes in NIBs and LIBs. However, unlike the intercalation of lithium or potassium, sodium is hardly intercalated between the graphite layers without any organic solvents. Therefore, it is impossible to substantiate NIBs using graphite as a negative electrode in the same manner as LIBs. In contrast, since the 1990's, it has been reported that sodium ions have been electrochemically doped into amorphous carbon (HC) electrodes.^[24] Currently, HC is expected to be the most promising electrode material for NIBs, because of its stable cyclability and high energy density.^[25] The capacity of sodium storage and the electronic state of stored sodium change depending on the internal HC structure,^[26] which varies depending on the precursor and heat treatment (carbonization) temperature.^[27]

Using ^{23}Na NMR, we investigated the state of sodium stored in HC samples prepared from sucrose by carbonization at various temperatures.^[28] HC prepared at approximately 1400–1700 °C showed the highest electrochemical capacity of Na, whereas HC heat-treated at lower temperatures (approximately 1000–1300 °C) was better for Li storage. Figure 6 shows the ^{23}Na MAS NMR spectra of fully sodiated HC (Na–HC) prepared by dehydration (in air: 180 °C) followed by carbonization at 1300 or 1600 °C. Each spectrum was optimized by superimposing two or three Lorentz components: i) a sharp signal at –9 to –10 ppm, attributed to the sodium salt in the electrolyte, ii) a broad signal between 5 and –15 ppm, with a FWHM of 20 ppm or more, and iii) a signal near 5 ppm. Alcántara et al.,^[29] and others^[30] reported that the components ii) and iii) were attributed to Na stored in the closed pores and Na inserted between the carbon layers of graphite-like structures in HC, respectively. However, ^{23}Na NMR analyses of several Na–HC

samples prepared from different precursors or different carbonization conditions in the past eight years have reported different shapes of the NMR spectra, depending on the internal HC structure, composition of the electrodes, and type of electrolyte solution. Furthermore, the second-order quadrupole effect of ^{23}Na , which is a quadrupole nucleus with spin ($I=3/2$), induces a shift in the peak and changes the signal form depending on the strength of the external magnetic field.^[31] Nevertheless, a broad signal between 5 and –20 ppm, corresponding to component (ii), has been observed in many previous studies. Hence, the broad component (ii) can be ascribed to the major component of Na inserted in the inner structure of general HCs, which may include both Na between the layers and within closed pores. The other components observed in each study were assigned to Na in other storage sites, and irreversible surface components including solid electrolyte interphase (SEI), electrolytes, and Na in the conductive assistant. ^{23}Na NMR signals of Na inserted in carbon nanotubes are also observed at –2~–28 ppm,^[32] which corresponded to component (ii).

The Na capacity of HC prepared at temperatures higher than 1700 °C generally decreases due to a reduction in the interlayer distances between the carbon layers (even with an increase in the average pore diameter of the closed pores). Additionally, the amount of Na adsorbed on the surface of the carbon layers is considered to be reduced because the number of functional groups and defective sites on the carbon surface decreases. A ^{23}Na multi-quantum (MQ) MAS NMR analysis shows that HC prepared from sucrose at 2000 °C has fewer storage sites than HC prepared at 1600 °C.^[28]

The charge/discharge curve of HC is roughly classified into two parts: a slope region (0.1 V or more), wherein the potential gradually changes with charge/discharge; and a plateau region (0.1 V or less), wherein the potential change is small. Conventionally, the capacity of the slope region is thought to correspond to the insertion of Na between the graphite-like layers of HC, and the capacity of the plateau region corresponds to the occlusion of Na in the closed pores of HC, when compared to the Li storage model^[24b,33] (Figure 7a). Recently, several new storage models have been proposed. Some researchers propose that Na is first adsorbed on the defect sites of carbon layers in HC and is subsequently stored between the carbon layers and closed pores^[34] (Figure 7b). Regarding the electrochemical insertion of Li into HC in LIBs, the signal of Li ions in HC is initially observed at 5–10 ppm during the slope region of lithiation (discharging a half cell); the peak gradually shifts to a higher frequency in the plateau region. The signal finally shifts to approximately 110 ppm in the fully lithiated state.^[35] This phenomenon is explained by a Knight shift of quasi-metallic lithium (clusters), formed in the internal pores of HC. A similar peak due to Knight shift was not observed for Na, but Stratford et al. (2016) reported that the signal shifted to over 700 ppm, which was ascribed to the quasi-metallic sodium cluster in HC, using *operando* ^{23}Na NMR measurements^[31a] (Figure 8).

Because quasi-metallic Na is observed only at the end of the sodiation stage, it is sometimes not clearly observed. For

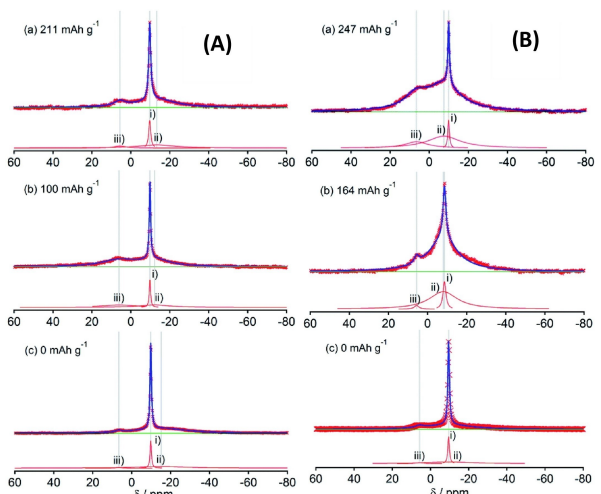


Figure 6. ^{23}Na MAS NMR spectra of sucrose-derived HC prepared by 1300 (A) and 1600 °C (B) at three different sodiation levels. Reproduced from Ref. [28] under the terms of the Creative Commons License. Copyright (2016) Royal Society of Chemistry..

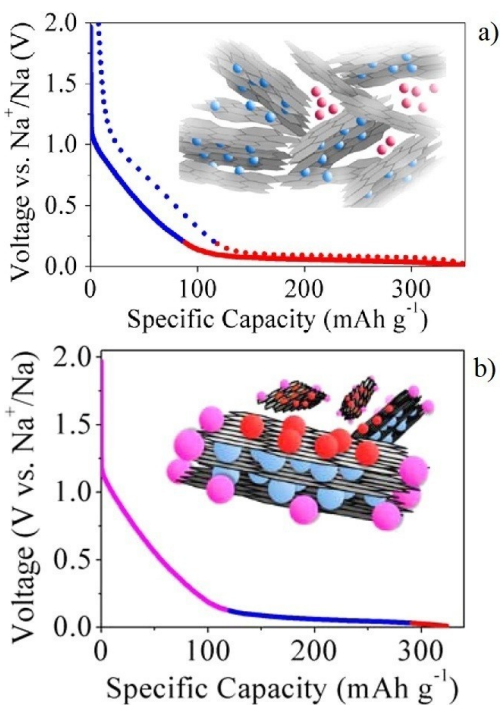


Figure 7. Proposed sodium storage mechanisms of HC. a) The traditional model from Stevens and Dahn, and b) the alternative model. Reprinted from Ref. [34a] with permission. Copyright (2015) American Chemical Society.

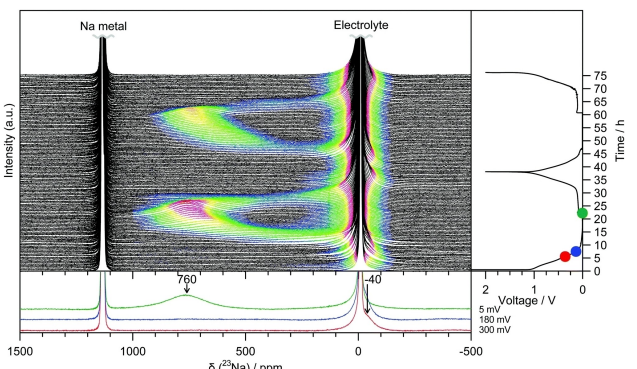


Figure 8. Operando ^{23}Na NMR spectra for an electrochemical cell with sodium metal and HC electrodes. Reproduced from Ref. [31a] under the terms of the Creative Commons License. Copyright (2016) Royal Society of Chemistry.

example, if the electrolyte contains fluoroethylene carbonate (FEC) as an additive or the Na capacity does not emerge due to deterioration of the electrolyte solution under insufficient atmospheric control, the sodiation potential quickly drops to 0 V and disturbs the formation of quasi-metallic Na. Nevertheless, a correlation between the metallic properties of the Na cluster (the peak of the quasi-metallic Na component) in the full sodiation state and the structure of HC has been reported.^[34b,36] Figure 9 shows the ^{23}Na NMR spectra of fully sodiated HC samples prepared by different dehydration (in air) temperatures and the subsequent carbonization (in nitrogen gas) temperatures.^[36] As shown in Figure 9 (c), the fully sodiated sample prepared at higher carbonization temperatures shows a

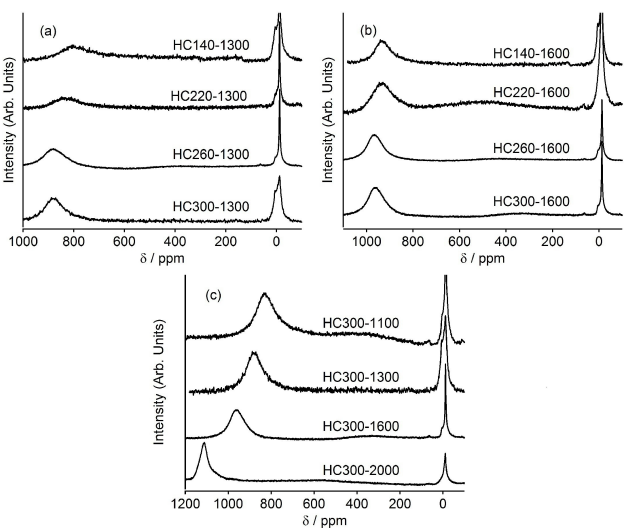


Figure 9. ^{23}Na NMR spectra of fully sodiated HC samples prepared by: a) dehydration at 140, 220, 260, or 300°C and subsequent carbonization at 1300°C, b) dehydration at 140–300°C followed by carbonization at 1600°C, and c) dehydration at 300°C followed by carbonization at 1100, 1300, 1600, or 2000°C. Reproduced from Ref. [36] with permission. Copyright (2019) Elsevier.

higher ^{23}Na NMR shift associated with Na clusters. Na in HC prepared at 2000°C shows a shift similar to that of the sodium metal. Furthermore, as shown in Figures 9(a) and (b), a higher dehydration temperature of the precursor favors the formation of Na clusters with a higher shift. This implies that the HC pore structure is not only influenced by the carbonization temperature but also by the heat treatment process.

Recently, sodium analyses have been conducted using *in situ* (*operando*) Na NMR or imaging (MRI) techniques. *Operando* NMR is a method of real-time analysis that conducts NMR acquisition by charging and discharging the battery simultaneously. *Operando* NMR^[37] and MRI^[38] have been applied to several ^7Li analyses of LIBs. For sodium analysis, Bray et al. visualized the distribution of Na ions and metallic Na in an NIB full cell using MRI^[39] (Figure 10). Bayley et al., Xiang et al., and Rees et al. observed the growth of Na dendrites in Na//Na cells or Na//Cu cells using *operando* ^{23}Na NMR^[40] or MRI (Figure 11).^[41] In the MRI analysis,^[41b] the spin-spin relaxation time (T_2) of the dendrite was found to be significantly longer than the T_2 of the bulk metal electrode, which is attributed to increased Na dynamics in the dendrite. We conducted an in-depth investigation of the oversodiation and subsequent desodiation of HC electrodes in the first cycle using *operando* ^{23}Na NMR and compared the behavior with overlithiation and delithiation of HC and graphite electrodes (Figure 12).^[42] The deposition of Na dendrites in HC started after the end of quasi-metallic sodium formation for oversodiation. The formation of quasi-metallic Na in the HC pores serves as a buffer for the metal plating that occurs when the batteries are overcharged.

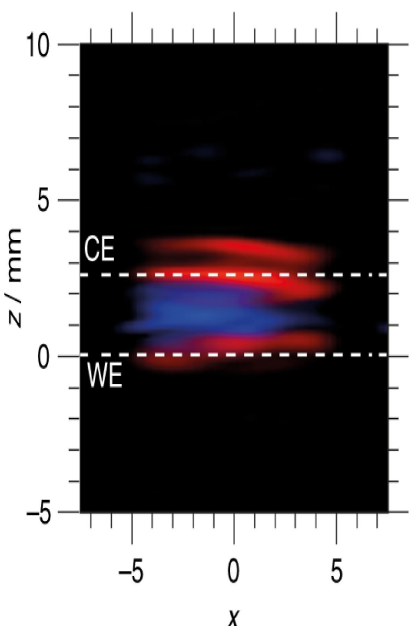


Figure 10. 2D ^{23}Na MRI of metallic (red) and dielectric (blue) sodium in the cell, after discharge at a specific current of 150 mA g^{-1} . The positions of the working electrode (WE) and the counter electrode (CE) are denoted. Reproduced from Ref. [39] under the terms of the Creative Commons License. Copyright (2020) Springer Nature.

3.2. Graphite

Graphite forms graphite intercalation compounds (GICs) by the insertion of guest molecules and ions between the graphene layers. Lithium-introduced graphite (binary Li-GIC) is commonly used as the negative electrode of LIBs in GIC. However, ternary GIC, wherein the organic electrolyte and lithium are co-intercalated, is not suitable for the negative electrode because of the exfoliation of graphene layers by charge/discharge cycles. In contrast to NIBs, it was reported in 2014 that anode materials of the ternary GIC system using a graphite electrode and diglyme (diethylene glycol dimethyl ether) solvent exhibit a 1000-fold superior cycle performance and capacity of ca. 100 mAh g^{-1} .^[43] Subsequently, the use of several linear and cyclic glyme solvents (mono-, di-, tri-, tetra-glyme, and crown ethers) have been reported.^[44] The orientation and dynamics of organic molecules intercalated between layers of ternary GICs have been investigated by wide-line ^1H or ^{2}H NMR. We measured the temperature dependence of the ^{2}H NMR spectrum of Na-deuterated diglyme (d14 -GIC synthesized chemically and revealed the dynamic behavior of diglyme molecules and sodium ions.^[45] The diglyme molecule fixedly coordinates to sodium at 233 K, even though the methyl group of diglyme is rotating. By contrast, the diglyme molecule rotates almost freely in the direction parallel to the graphite layer with weak coordination to an Na ion through the central oxygen atom at room temperature (Figure 13). The rotational motion and diffusion of molecules observed by NMR are local and do not directly correspond to the macroscopic diffusion of molecules over long distances. However, because long-distance diffusion is based on the local molecular motion and diffusion,

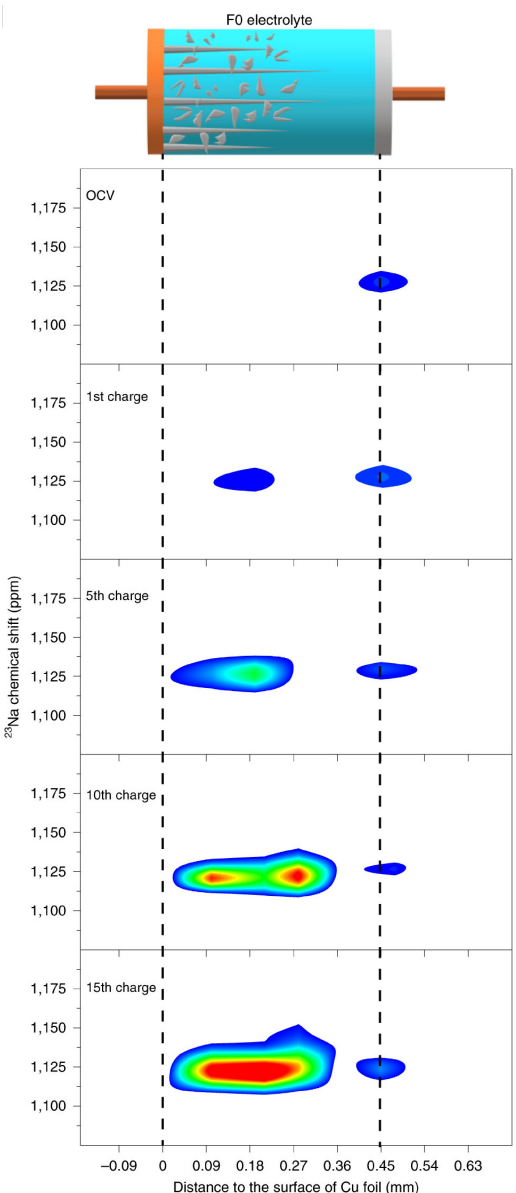


Figure 11. ^{23}Na metal MRI images of an Na//Cu battery at OCV and 1st–15th cycles. Reproduced from Ref. [41a] with permission. Copyright (2020) Springer Nature.

the considerably free local behavior of the molecule observed by ^2H NMR at room temperature is beneficial for the diffusion of Na-diglyme in the intralayer space. This explains why NIBs using this compound can be charged and discharged at a high rate. The diglyme coordinating to Na in the graphite layers was also analyzed by high-resolution ^1H and ^{13}C NMR.^[46] Cross-polarization (CP) dynamic measurements demonstrated that the Na-(diglyme)₂ complex is weak when interacting with the graphene sheets, as compared to Li-(diglyme)₂. The dynamics of intercalated Na-(diglyme)₂ have some translational characters, in accordance with lateral diffusivity and weaker binding to the graphite electrons, whereas the Li-(diglyme)₂ only displays the rotational character (Figure 14).

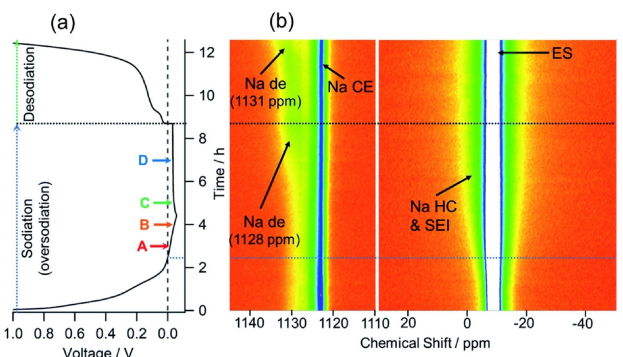


Figure 12. a) Discharge (oversodiation) and following charge (desodiation) profiles of HC/Na cell in the first cycle, and b) the corresponding *operando* ^{23}Na NMR spectra. The formation of Na dendrite (Na de) peaks starts after the minimum of the potential curve. The quasi-metallic sodium is observed after point B on the curve by *ex situ* NMR spectra. Reproduced from Ref. [42] with permission. Copyright (2020) Royal Society of Chemistry.

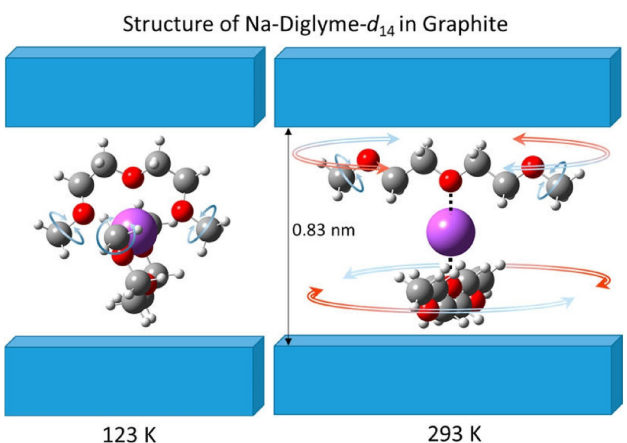


Figure 13. Models of diglyme and sodium (purple sphere) in graphite, a) at 123 K and b) at ambient temperature, derived from ^2H NMR spectrum analyses. Reprinted from Ref. [45] with permission. Copyright (2016) American Chemical Society.

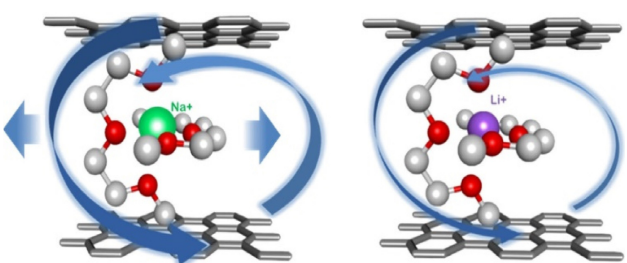


Figure 14. Models of the motions of the Na-(diglyme)₂ (left) and Li-(diglyme)₂ (right) derived from ^1H and ^{13}C NMR analyses. Reprinted from Ref. [46] with permission. Copyright (2018) American Chemical Society.

3.3. Other Anode Materials (Metals, Phosphorus, and 2D Inorganic Materials)

As in the case of LIBs, carbon, as well as various other materials, can be used as negative electrode materials for NIBs. In particular, phosphorus (P), inorganic layered materials, and metal electro-

des, such as antimony (Sb) and tin (Sn), were analyzed using NMR. When sodium is electrochemically introduced into the negative electrode material of a metal or inorganic material, an alloy comprising Na and an electrode material is formed by the electrochemical reaction. During sodiation and desodiation, the compound forms structures with different compositions. Some of them have a stable crystalline structure, but the compounds form an amorphous structure in many instances. As it is difficult to analyze the non-crystalline state using XRD, NMR is frequently employed by combining theoretical calculations of the chemical shift value and atomic pair distribution function (PDF) analysis of XRD.

In the Sb electrode, Na_3Sb is formed at full sodiation. Na_{3-x}Sb ($0.4 < x < 0.5$) (with a local structure similar to that of Na_3Sb) and amorphous $\text{Na}_{1.7}\text{Sb}$ appear as intermediate phases between the fully sodiated (Na_3Sb) and desodiated (Sb) states (Figure 15).^[47] For the Sn negative electrode, it varies through considerably complicated reactions with sodium, as shown in Figure 16(a).^[48] $\text{Na}_{15+x}\text{Sn}_4$ has been proposed as the final sodiated composition, which contains more Na ions than the stable crystalline state of $\text{Na}_{15}\text{Sn}_4$. In the ^{23}Na NMR analysis, peaks at 620 ppm (NaSn_2) in Process 1, 75–50 ppm ($\text{Na}_{1.2}\text{Sn}$ as the major component) in Process 2, 202–180 ppm (mainly $\text{Na}_{4.4}\text{Sn}$ to $\text{Na}_{4.75}\text{Sn}$) in Process 3, and –75 and –260 ppm (mainly $\text{Na}_{15}\text{Sn}_4$ and $\text{Na}_{15+x}\text{Sn}_4$) in Process 4 were observed. Basically, the chemical shift value of the signal gradually moves to a lower frequency under the influence of the Knight shift, whereas a retrograde shift occurs between Processes 2 and 3 (Figure 16 (b)).

Phosphorus is known to have a particularly high capacity among various negative electrode materials. The theoretical capacity of Na_3P , which is a fully sodiated structure, is 2596 mAh g^{-1} .^[49] Among the six different compounds of sodium phosphide predicted by the first-principles calculations,^[50] five compounds (NaP_7 , Na_3P_{11} , Na_3P_7 , NaP , and Na_3P) have been identified experimentally. These compounds can be synthesized by the reaction of Na metal and phosphorus in the solid phase.^[51] However, regarding electrochemical reactions, some studies reported that no crystalline state apart from Na_3P appears during the sodiation of phosphorous.^[51b,52] The presence of at least three environments with associated ^{31}P NMR shifts at –29, –78, and –143 ppm, corresponding to $\alpha\text{-Na}_x\text{P}$ is confirmed for a sample of approximate NaP composition (Figure 17). The reaction pathways in sodiation and desodiation are considerably different in the first cycle,^[52] but they become a reversible reaction after three cycles.^[51b] During the first sodiation, analysis of the ^{31}P chemical shift anisotropies in the NMR data revealed P helices and P at the end of chains as the primary structural components in amorphous Na_xP phases. XRD data in conjunction with variable field ^{23}Na MAS NMR support the formation of a new Na_3P crystal structure ($P6_{3}/cm$) on sodiation.^[52] The P electrode goes through three types of amorphous $\text{Na}_{1-\alpha}\text{P}$, $\text{Na}_{2-\beta}\text{P}$, and $\text{Na}_{3-\gamma}\text{P}$ ($0 < \alpha, \beta, \gamma < 1$) during the charging and discharging process in the fourth cycle (Figure 18).^[51b] The formation of the Na_3P crystalline structure has also been confirmed in the sodiated vanadium dishosphide (VP_2) electrode, using ^{23}Na NMR.^[53]

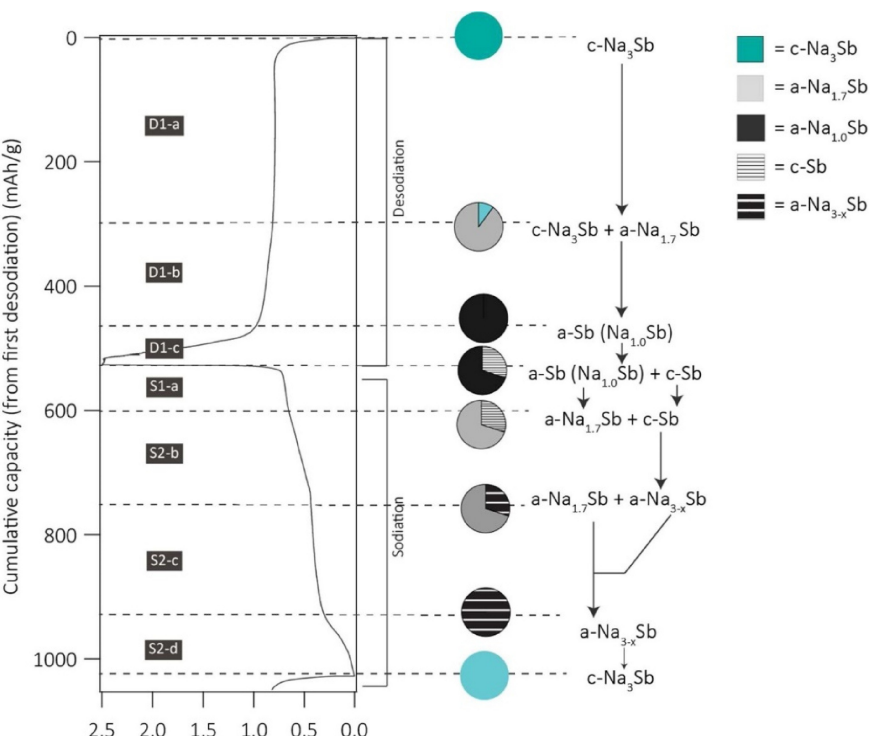


Figure 15. NMR and PDF-derived mechanism of (de)sodiation of antimony after the first desodiation during galvanostatic cycling at a rate of C/20. Reprinted from Ref. [47] with permission. Copyright (2016) American Chemical Society.

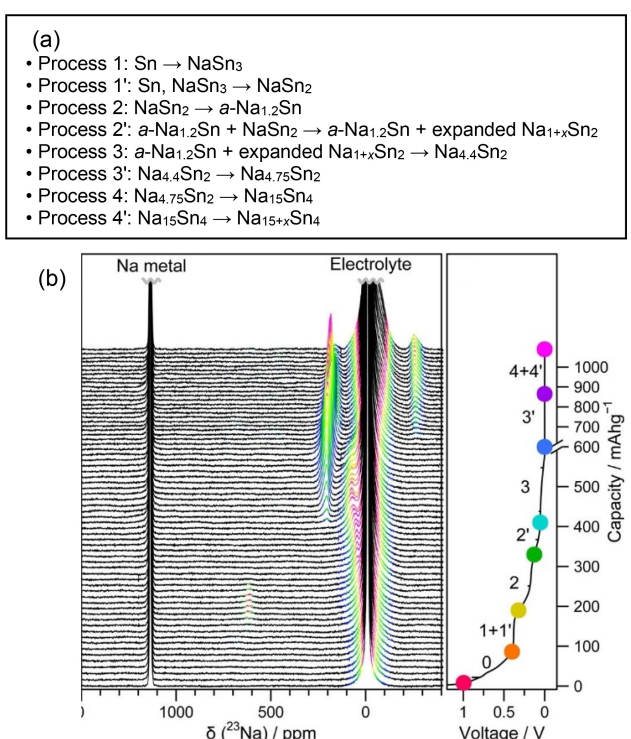


Figure 16. a) Discharge reaction mechanism of Na_xSn proposed by PDF, XRD, and NMR analyses, and b) ²³Na *operando* NMR spectra obtained from the first discharge. Reprinted from Ref. [48] with permission. Copyright (2017) American Chemical Society.

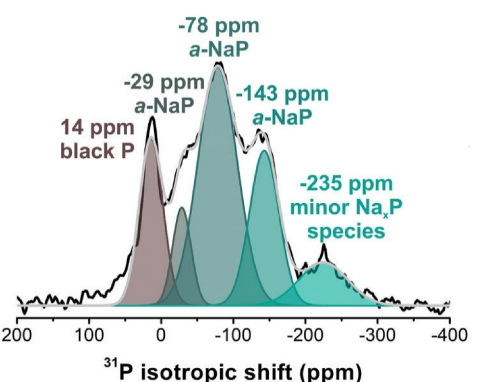


Figure 17. Deconvolution of the ³¹P isotropic projection from 2D ³¹P PASS NMR experiments (black line) performed on a sample of approximate composition NaP, extracted from a NIB at 0.38 V (780 mAh g⁻¹) during the first sodiation. Reprinted from Ref. [52] with permission. Copyright (2018) American Chemical Society.

The ternary Na/Si/P system of phosphorous silicide was also investigated using ³¹P, ²³Na, and ¹⁹F MAS NMR and XRD to compare lithiated Li/Si/P. The P–P bonds and SiP₄ tetrahedra connections are not broken upon discharge, and the structure of the pristine SiP₂ maintains its integrity throughout the electrochemical cycling.^[54]

Various inorganic materials have been proposed as intercalation-type negative electrode materials apart from carbon materials. Two-dimensional nanosheet materials, called MXenes, have been proposed as promising materials. One of the MXene compounds, Ti₃C₂T_x (T_x: the functional termination

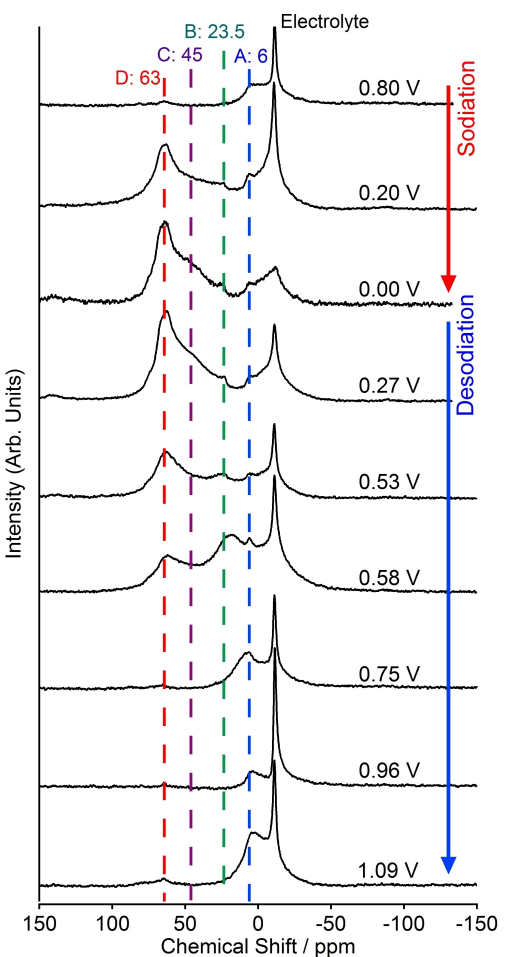


Figure 18. *Ex situ* ^{23}Na MAS NMR spectra (10 kHz spinning) of Na–P compounds at the fourth cycle. The signal A, B, C, and D correspond to $\text{Na}_{1-\alpha}\text{P}$, $\text{Na}_{2-\beta}\text{P}$, $\text{Na}_{3-\gamma}\text{P}$ ($0 < \alpha, \beta, \gamma < 1$) and Na_3P , respectively. Reproduced from Ref. [51b] with permission. Copyright (2019) Elsevier.

group) was analyzed using NMR. ^1H and ^{13}C NMR were used to analyze the surface functional groups of the material.^[55] The change in state of Na owing to charge and discharge was observed by ^{23}Na NMR and XRD to elucidate the charge and discharge mechanism (Figure 19).^[56] $\text{Ti}_3\text{C}_2\text{T}_x$ undergoes expansion of the interlayer distance during the first sodiation, whereby desolvated Na^+ is intercalated and deintercalated reversibly.

In other examples, the moisture and water stability of the titanium-based oxide anode, $\text{Na}_2\text{Ti}_3\text{O}_7$ has been investigated using ^{23}Na MQMAS NMR and ^1H NMR.^[57]

4. Conclusions

The stable sodiation/desodiation cycle of NIB was first reported 10 years ago by the author and Komaba et al.^[25a] Research in the field of NIBs has grown gradually. Analytical research using NMR has been conducted since the early stages of sodium battery development, and the number of publications has increased rapidly since 2016. Currently, the range of research

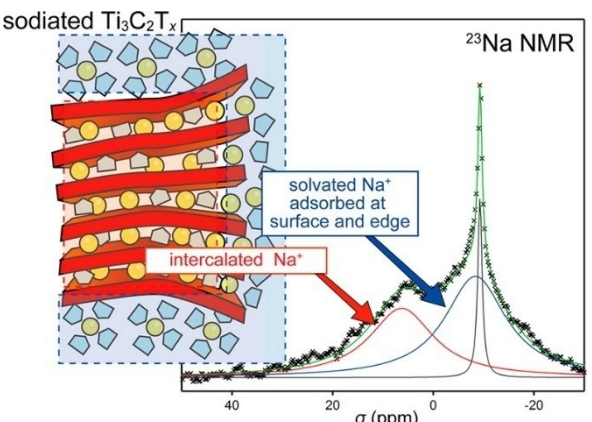


Figure 19. A structure model of sodiated MXene ($\text{Ti}_3\text{C}_2\text{T}_x$) and the deconvoluted ^{23}Na NMR spectra. Reprinted from Ref. [56] with permission. Copyright (2016) American Chemical Society.

has expanded to various materials. Research papers using NMR on carbon-based negative electrode materials are frequently reported, and a number of positive electrode materials and alloy-based negative electrode materials have also been investigated. However, most of these still require detailed analysis regarding the development of materials.

There are still some difficulties in NMR analysis of NIBs and related sodium insertion materials. For example, most electrodes in NIBs are extremely sensitive to moisture and oxygen in the atmosphere and are easily decomposed. Additionally, some electrode materials, such as paramagnetic positive electrodes, require the analysis of high-speed MAS and a lower magnetic field, as stated in the introduction. In most cases, the interpretation of the NMR spectra requires a different discussion for each material. However, the characteristic of NMR, which can analyze the amorphous state, is particularly useful in the analysis of battery materials. The use of state-of-the-art NMR technologies to enhance the signal intensity, such as an extremely high field magnet (1.2 GHz or more), cryogenic probe, and dynamic nuclear polarization (DNP), will help in the detection of tiny amounts of impurities and imperceptible changes in the electrodes. Thus, NMR will be advantageous to the analysis of numerous battery materials in the future.

Acknowledgements

The author is grateful to Professor Shinichi Komaba, Tokyo University of Science, and Professor Hiroyuki Ishida, Okayama University, for several important suggestions and valuable discussions. This work was supported by JSPS Grants-in-Aid for Scientific Research (KAKENHI) No. 17K06017.

Conflict of Interest

The authors declare no conflict of interest.

Keywords: sodium-ion battery · nuclear magnetic resonance · cathode · anode

- [1] a) B. L. Ellis, L. F. Nazar, *Curr. Opin. Solid State Mater. Sci.* **2012**, *16*, 168; b) V. Palomares, P. Serras, I. Villaluenga, K. B. Hueso, J. Carretero-Gonzalez, T. Rojo, *Energy Environ. Sci.* **2012**, *5*, 5884; c) H. Pan, Y.-S. Hu, L. Chen, *Energy Environ. Sci.* **2013**, *6*, 2338; d) M. D. Slater, D. Kim, E. Lee, M. Doeff, C. S. Johnson, *Adv. Funct. Mater.* **2013**, *23*, 947; e) M. Dahbi, N. Yabuuchi, K. Kubota, K. Tokiwa, S. Komaba, *Phys. Chem. Chem. Phys.* **2014**, *16*, 15007; f) N. Yabuuchi, K. Kubota, M. Dahbi, S. Komaba, *Chem. Rev.* **2014**, *114*, 11636; g) K. Kubota, S. Komaba, *J. Electrochem. Soc.* **2015**, *162*, A2538; h) D. Kundu, E. Talaie, V. Duffort, L. F. Nazar, *Angew. Chem. Int. Ed.* **2015**, *54*, 3431; i) L. P. Wang, L. Yu, X. Wang, M. Srinivasan, Z. J. Xu, *J. Mater. Chem. A* **2015**, *3*, 9353; j) W. Luo, F. Shen, C. Bommier, H. Zhu, X. Ji, L. Hu, *Acc. Chem. Res.* **2016**, *49*, 231; k) J.-Y. Hwang, S.-T. Myung, Y.-K. Sun, *Chem. Soc. Rev.* **2017**, *46*, 3529; l) C. Delmas, *Adv. Energy Mater.* **2018**, *8*, 1703137; m) K. Kubota, M. Dahbi, T. Hosaka, S. Kumakura, S. Komaba, *Chem. Rec.* **2018**, *18*, 459; n) P. K. Nayak, L. Yang, W. Brehm, P. Adelhelm, *Angew. Chem. Int. Ed.* **2018**, *57*, 102; o) S. Komaba, *Chem. Lett.* **2020**, *49*, 1507.
- [2] K. Kubota, S. Kumakura, Y. Yoda, K. Kuroki, S. Komaba, *Adv. Energy Mater.* **2018**, *8*, 1703415.
- [3] a) J. Billaud, R. J. Clément, A. R. Armstrong, J. Canales-Vazquez, P. Rozier, C. P. Grey, P. G. Bruce, *J. Am. Chem. Soc.* **2014**, *136*, 17243; b) R. J. Clément, D. S. Middlemiss, I. D. Seymour, A. J. Ilott, C. P. Grey, *Chem. Mater.* **2016**, *28*, 8228.
- [4] R. J. Clément, J. Billaud, A. R. Armstrong, G. Singh, T. Rojo, P. G. Bruce, C. P. Grey, *Energy Environ. Sci.* **2016**, *9*, 3240.
- [5] D. Sehrawat, S. Cheong, A. Rawal, A. M. Glushenkov, H. E. A. Brand, B. Cowie, E. Gonzalo, T. Rojo, P. J. P. Naeyaert, C. D. Ling, M. Avdeev, N. Sharma, *CrystEngComm* **2019**, *21*, 172.
- [6] J. Cabana, N. A. Chernova, J. Xiao, M. Roppolo, K. A. Aldi, M. S. Whittingham, C. P. Grey, *Inorg. Chem.* **2013**, *52*, 8540.
- [7] C. Ma, J. Alvarado, J. Xu, R. J. Clément, M. Kodur, W. Tong, C. P. Grey, Y. S. Meng, *J. Am. Chem. Soc.* **2017**, *139*, 4835.
- [8] R. J. Clément, J. Xu, D. S. Middlemiss, J. Alvarado, C. Ma, Y. S. Meng, C. P. Grey, *J. Mater. Chem. A* **2017**, *5*, 4129.
- [9] a) M. H. Han, N. Sharma, E. Gonzalo, J. C. Pramudita, H. E. A. Brand, J. M. López del Amo, T. Rojo, *J. Mater. Chem. A* **2016**, *4*, 18963; b) M. Zarzabeitia, E. Gonzalo, M. Pasqualini, M. Ciambesi, O. Lakuntza, F. Nobili, A. Trapananti, A. Di Cicco, G. Aquilanti, N. A. Katcho, J. M. López del Amo, J. Carrasco, M. A. Muñoz-Márquez, T. Rojo, *J. Mater. Chem. A* **2019**, *7*, 14169; c) J. H. Stansby, W. M. Dose, N. Sharma, J. A. Kimpton, J. M. Lopez del Amo, E. Gonzalo, T. Rojo, *Electrochim. Acta* **2020**, *341*, 135978.
- [10] X. Liu, G. Zhong, Z. Xiao, B. Zheng, W. Zuo, K. Zhou, H. Liu, Z. Liang, Y. Xiang, Z. Chen, G. F. Ortiz, R. Fu, Y. Yang, *Nano Energy* **2020**, *76*, 104997.
- [11] D. Sehrawat, A. Rawal, S. Cheong, N. Sharma, *ACS Omega* **2019**, *4*, 5784.
- [12] E. Gonzalo, N. Ortiz-Vitoriano, N. E. Drewett, B. Acebedo, J. M. Lopez del Amo, F. J. Bonilla, T. Rojo, *J. Power Sources* **2018**, *401*, 117.
- [13] L. Yang, J. M. López del Amo, Z. Shadike, S.-M. Bak, F. Bonilla, M. Galceran, P. K. Nayak, J. R. Buchheim, X.-Q. Yang, T. Rojo, P. Adelhelm, *Adv. Funct. Mater.* **2020**, *30*, 2003364.
- [14] P. Serras, V. Palomares, T. Rojo, in *Alkali-ion Batteries*, DOI: 10.5772/62317 **2016**, Ch. 8, p. 155.
- [15] P. R. Kumar, Y. H. Jung, C. H. Lim, D. K. Kim, *J. Mater. Chem. A* **2015**, *3*, 6271.
- [16] C. Li, M. Shen, B. Hu, X. Lou, X. Zhang, W. Tong, B. Hu, *J. Mater. Chem. A* **2019**, *6*, 8340.
- [17] Z. Liu, Y.-Y. Hu, M. T. Dunstan, H. Huo, X. Hao, H. Zou, G. Zhong, Y. Yang, C. P. Grey, *Chem. Mater.* **2014**, *26*, 2513.
- [18] T. Broux, T. Bamine, L. Simonelli, L. Stievano, F. Fauth, M. Ménétrier, D. Carlier, C. Masquelier, L. Croguennec, *J. Phys. Chem. C* **2017**, *121*, 4103.
- [19] C. Li, M. Shen, X. Lou, B. Hu, *J. Phys. Chem. C* **2018**, *122*, 27224.
- [20] Z. Liang, R. Liu, Y. Xiang, J. Zhu, X. Liu, G. F. Ortiz, Y. Yang, *Electrochim. Acta* **2020**, *351*, 136454.
- [21] a) Q. Li, R. Liu, G. Zhong, X. Hou, Y. Yang, Z. Liu, J. Lee, P. Grey Clare, Z. Liu, Z. Liu, F. Zheng, S. Wu, G.-L. Xu, Z. Chen, K. Amine, G. Zhong, R. Fu, K. Amine, J. Mi, *Angew. Chem. Int. Ed.* **2018**, *57*, 11918; b) D. L. Smiley, D. Carlier, G. R. Goward, *Solid State Nucl. Magn. Reson.* **2019**, *103*, 1.
- [22] D. L. Smiley, G. R. Goward, *Chem. Mater.* **2016**, *28*, 7645.
- [23] V. Palomares, A. Iturrondobeitia, P. Sanchez-Fontecoba, D. Goonetilleke, N. Sharma, L. Lezama, T. Rojo, *Inorg. Chem.* **2020**, *59*, 854.
- [24] a) M. M. Doeff, Y. P. Ma, S. J. Visco, L. C. Dejonghe, *J. Electrochem. Soc.* **1993**, *140*, L169; b) D. A. Stevens, J. R. Dahn, *J. Electrochem. Soc.* **2000**, *147*, 1271; c) P. Thomas, D. Billaud, *Electrochim. Acta* **2002**, *47*, 3303.
- [25] a) S. Komaba, W. Murata, T. Ishikawa, N. Yabuuchi, T. Ozeki, T. Nakayama, A. Ogata, K. Gotoh, K. Fujiwara, *Adv. Funct. Mater.* **2011**, *21*, 3859; b) G. Hasegawa, K. Kanamori, N. Kannari, J.-i. Ozaki, K. Nakanishi, T. Abe, *ChemElectroChem* **2015**, *2*, 1917; c) H. Yamamoto, S. Muratsubaki, K. Kubota, M. Fukunishi, H. Watanabe, J. Kim, S. Komaba, *J. Mater. Chem. A* **2018**, *6*, 16844.
- [26] B. Xiao, T. Rojo, X. Li, *ChemSusChem* **2019**, *12*, 133.
- [27] a) J. Górká, C. Vix-Guterl, C. M. Ghimbeu, *C* **2016**, *2*, 24; b) X. Dou, I. Hasa, D. Saurel, C. Vaalma, L. Wu, D. Buchholz, D. Bresser, S. Komaba, S. Passerini, *Mater. Today* **2019**, *23*, 87.
- [28] R. Morita, K. Gotoh, M. Fukunishi, K. Kubota, S. Komaba, N. Nishimura, T. Yumura, K. Deguchi, S. Ohki, T. Shimizu, H. Ishida, *J. Mater. Chem. A* **2016**, *4*, 13183.
- [29] R. Alcántara, P. Lavela, G. F. Ortiz, J. L. Tirado, *Electrochim. Solid-State Lett.* **2005**, *8*, A22.
- [30] a) K. Gotoh, T. Ishikawa, S. Shimadzu, N. Yabuuchi, S. Komaba, K. Takeda, A. Goto, K. Deguchi, S. Ohki, K. Hashi, T. Shimizu, H. Ishida, *J. Power Sources* **2013**, *225*, 137; b) Z. Zheng, Q. Su, Q. Zhang, H. Ye, Z. Wang, *J. Mater. Sci.* **2018**, *53*, 12421.
- [31] a) J. M. Stratford, P. K. Allan, O. Pecher, P. A. Chater, C. P. Grey, *Chem. Commun.* **2016**, *52*, 12430; b) D. C. Apperley, R. K. Harris, P. Hodgkinson, *Solid-State NMR: Basic Principles & Practice*, Momentum Press, 2012.
- [32] D. Goonetilleke, J. C. Pramudita, M. Choucair, A. Rawal, N. Sharma, *J. Power Sources* **2016**, *314*, 102.
- [33] a) H. Alptekin, H. Au, A. C. S. Jensen, E. Olsson, M. Goktas, T. F. Headen, P. Adelhelm, Q. Cai, A. J. Drew, M.-M. Titirici, *ACS Appl. Mater. Interfaces* **2020**, *3*, 9918; b) H. Lu, F. Ai, Y. Jia, C. Tang, X. Zhang, Y. Huang, H. Yang, Y. Cao, *Small* **2018**, *14*, n/a; c) Z.-E. Yu, Y. Lyu, Y. Wang, S. Xu, H. Cheng, X. Mu, J. Chu, R. Chen, Y. Liu, B. Guo, *Chem. Commun.* **2020**, *56*, 778.
- [34] a) C. Bommier, T. W. Surta, M. Dolgos, X. Ji, *Nano Lett.* **2015**, *15*, 5888; b) H. Au, H. Alptekin, A. C. S. Jensen, E. Olsson, C. A. O'Keefe, T. Smith, M. Crespo-Ribadeneyra, T. F. Headen, C. P. Grey, Q. Cai, A. J. Drew, M.-M. Titirici, *Energy Environ. Sci.* **2020**, *13*, 3469; c) M. Anji Reddy, M. Helen, A. Groß, M. Fichtner, H. Euchner, *ACS Energy Lett.* **2018**, *3*, 2851; d) S. Alvin, D. Yoon, C. Chandra, H. S. Cahyadi, J.-H. Park, W. Chang, K. Y. Chung, J. Kim, *Carbon* **2019**, *145*, 67; e) S. Alvin, H. S. Cahyadi, J. Hwang, W. Chang, S. K. Kwak, J. Kim, *Adv. Energy Mater.* **2020**, *10*, 2000283; f) B.-H. Hou, Y.-Y. Wang, Q.-L. Ning, W.-H. Li, X.-T. Xi, X. Yang, H.-J. Liang, X. Feng, X.-L. Wu, *Adv. Mater.* **2019**, *31*, 1903125; g) Y. Jin, S. Sun, M. Ou, Y. Liu, C. Fan, X. Sun, J. Peng, Y. Li, Y. Qiu, P. Wei, Z. Deng, Y. Xu, J. Han, Y. Huang, *ACS Appl. Mater. Interfaces* **2018**, *1*, 2295; h) Z. Li, C. Bommier, Z. S. Chong, Z. Jian, T. W. Surta, X. Wang, Z. Xing, J. C. Neuefeind, W. F. Stickle, M. Dolgos, P. A. Greaney, X. Ji, *Adv. Energy Mater.* **2017**, *7*, 1602894; i) C. Matei Ghimbeu, J. Gorká, V. Simone, L. Simonin, S. Martinet, C. Vix-Guterl, *Nano Energy* **2018**, *44*, 327; j) Y. Morikawa, S. Nishimura, R. Hashimoto, M. Ohnuma, A. Yamada, *Adv. Energy Mater.* **2020**, *10*, 1903176; k) D. Saurel, B. Orayech, B. Xiao, D. Carriazo, X. Li, T. Rojo, *Adv. Energy Mater.* **2018**, *8*, 1703268.
- [35] a) K. Tatsumi, J. Conard, M. Nakahara, S. Menu, P. Lauginie, Y. Sawada, Z. Ogumi, *Chem. Commun.* **1997**, 687; b) K. Gotoh, M. Maeda, A. Nagai, A. Goto, M. Tansho, K. Hashi, T. Shimizu, H. Ishida, *J. Power Sources* **2006**, *162*, 1322.
- [36] R. Morita, K. Gotoh, K. Kubota, S. Komaba, K. Hashi, T. Shimizu, H. Ishida, *Carbon* **2019**, *145*, 712.
- [37] a) M. Letellier, F. Chevallier, C. Clinard, E. Frackowiak, J.-N. Rouzaud, F. Béguin, M. Morcrette, J.-M. Tarascon, *J. Chem. Phys.* **2003**, *118*, 6038; b) N. M. Trease, T. K. J. Koster, C. P. Grey, *Electrochim. Soc. Interface* **2011**, *20*, 69; c) F. Blanc, M. Leskes, P. Grey Clare, *Acc. Chem. Res.* **2013**, *46*, 1952; d) M. Letellier, *Encycl. Spectrosc. Spectrom.* **2017**, *2*, 181; e) O. Pecher, J. Carretero-González, K. J. Griffith, C. P. Grey, *Chem. Mater.* **2017**, *29*, 213; f) Z. Hu Jian, R. Jaegers Nicholas, Y. Hu Mary, T. Mueller Karl, *J. Phys. Condens. Matter* **2018**, *30*, 463001; g) S. A. Kayser, A. Mester, A. Mertens, P. Jakes, R.-A. Eichel, J. Granwehr, *Phys. Chem. Chem. Phys.* **2018**, *20*, 13765; h) S. A. Krachkovskiy, J. M. Foster, J. D. Bazak, B. J. Balcom, G. R. Goward, *J. Phys. Chem. C* **2018**, *122*, 21784; i) K. Kitada, O. Pecher, P. C. M. M. Magusin, M. F. Groh, R. S. Weatherup, C. P. Grey, *J. Am. Chem. Soc.* **2019**, *141*, 7014; j) K. Märker, C. Xu, C. P. Grey, *J. Am. Chem. Soc.* **2020**, *142*, 17447.
- [38] a) N. Kuwata, Y. Iwai, J. Kawamura, *Mater. Integr.* **2011**, *24*, 172; b) S. Chandrashekhar, N. M. Trease, H. J. Chang, L.-S. Du, C. P. Grey, A. Jerschow, *Nat. Mater.* **2012**, *11*, 311; c) H. J. Chang, A. J. Ilott, N. M.

- Trease, M. Mohammadi, A. Jerschow, C. P. Grey, *J. Am. Chem. Soc.* **2015**, 137, 15209; d) S. Chandrashekhar, O. Oparaji, G. Yang, D. Hallinan Jr., *J. Electrochem. Soc.* **2016**, 163, A2988; e) A. J. Ilott, M. Mohammadi, H. J. Chang, C. P. Grey, A. Jerschow, *Proc. Natl. Acad. Sci. USA* **2016**, 113, 10779; f) K. Romanenko, L. Jin, P. Howlett, M. Forsyth, *Chem. Mater.* **2016**, 28, 2844; g) P.-H. Chien, X. Feng, M. Tang, J. T. Rosenberg, S. Oneill, J. Zheng, S. C. Grant, Y.-Y. Hu, *J. Phys. Chem. Lett.* **2018**, 9, 1990; h) L. E. Marbella, S. Zekoll, J. Kasemchainan, S. P. Emge, P. G. Bruce, C. P. Grey, *Chem. Mater.* **2019**, 31, 2762; i) M. Mohammadi, A. Jerschow, *J. Magn. Reson.* **2019**, 308, 106600;j) R. Pigliapochi, S. Benders, E. V. Silletta, S. L. Glazier, E. Lee, J. Dahn, A. Jerschow, *Batteries Supercaps* **2020**, 4, 322.
- [39] J. M. Bray, C. L. Doswell, G. E. Pavlovskaya, L. Chen, B. Kishore, H. Au, H. Alptekin, E. Kendrick, M.-M. Titirici, T. Meersmann, M. M. Britton, *Nat. Commun.* **2020**, 11, 2083.
- [40] P. M. Bayley, N. M. Trease, C. P. Grey, *J. Am. Chem. Soc.* **2016**, 138, 1955.
- [41] a) Y. Xiang, G. Zheng, Z. Liang, Y. Jin, X. Liu, S. Chen, K. Zhou, J. Zhu, M. Lin, H. He, J. Wan, S. Yu, G. Zhong, R. Fu, Y. Li, Y. Yang, *Nat. Nanotechnol.* **2020**, 15, 883; b) G. J. Rees, D. S. Jolly, Z. Ning, T. J. Marrow, G. E. Pavlovskaya, P. G. Bruce, *Angew. Chem. Int. Ed.* **2021**, 60, 2110.
- [42] K. Gotoh, T. Yamakami, I. Nishimura, H. Kometani, H. Ando, K. Hashi, T. Shimizu, H. Ishida, *J. Mater. Chem. A* **2020**, 8, 14472.
- [43] a) B. Jache, P. Adelhelm, *Angew. Chem. Int. Ed.* **2014**, 53, 10169; b) H. Kim, J. Hong, Y.-U. Park, J. Kim, I. Hwang, K. Kang, *Adv. Funct. Mater.* **2015**, 25, 534.
- [44] a) Y. Li, Y. Lu, P. Adelhelm, M.-M. Titirici, Y.-S. Hu, *Chem. Soc. Rev.* **2019**, 48, 4655; b) M. Goktas, C. Bolli, J. Buchheim, E. J. Berg, P. Novák, F. Bonilla, T. Rojo, S. Komaba, K. Kubota, P. Adelhelm, *ACS Appl. Mater. Interfaces* **2019**, 11, 32844; c) M. Goktas, C. Bolli, E. J. Berg, P. Novák, K. Pollok, F. Langenhorst, M. v Roeder, O. Lenchuk, D. Mollenhauer, P. Adelhelm, *Adv. Energy Mater.* **2018**, 8, 1702724; d) M. Goktas, B. Akduman, P. Huang, A. Balducci, P. Adelhelm, *J. Phys. Chem. C* **2018**, 122, 26816; e) L. Seidl, N. Bucher, E. Chu, S. Hartung, S. Martens, O. Schneider, U. Stimming, *Energy Environ. Sci.* **2017**, 10, 1631; f) S. C. Jung, Y.-J. Kang, Y.-K. Han, *Nano Energy* **2017**, 34, 456; g) B. Jache, J. O. Binder, T. Abe, P. Adelhelm, *Phys. Chem. Chem. Phys.* **2016**, 18, 14299; h) H. Kim, J. Hong, G. Yoon, H. Kim, K.-Y. Park, M.-S. Park, W.-S. Yoon, K. Kang, *Energy Environ. Sci.* **2015**, 8, 2963.
- [45] K. Gotoh, H. Maruyama, T. Miyatou, M. Mizuno, K. Urita, H. Ishida, *J. Phys. Chem. C* **2016**, 120, 28152.
- [46] N. Leifer, M. F. Greenstein, A. Mor, D. Aurbach, G. Goobes, *J. Phys. Chem. C* **2018**, 122, 21172.
- [47] P. K. Allan, J. M. Griffin, A. Darwiche, O. J. Borkiewicz, K. M. Wiaderek, K. W. Chapman, A. J. Morris, P. J. Chupas, L. Monconduit, C. P. Grey, *J. Am. Chem. Soc.* **2016**, 138, 2352.
- [48] J. M. Stratford, M. Mayo, P. K. Allan, O. Pecher, O. J. Borkiewicz, K. M. Wiaderek, K. W. Chapman, C. J. Pickard, A. J. Morris, C. P. Grey, *J. Am. Chem. Soc.* **2017**, 139, 7273.
- [49] a) J. Ni, L. Li, J. Lu, *ACS Energy Lett.* **2018**, 3, 1137; b) J. Qian, X. Wu, Y. Cao, X. Ai, H. Yang, *Angew. Chem. Int. Ed.* **2013**, 52, 4633; c) M. Dahbi, N. Yabuuchi, M. Fukunishi, K. Kubota, K. Chihara, K. Tokiwa, X.-F. Yu, H. Ushiyama, K. Yamashita, J.-Y. Son, Y.-T. Cui, H. Oji, S. Komaba, *Chem. Mater.* **2016**, 28, 1625; d) N. Yabuuchi, Y. Matsuura, T. Ishikawa, S. Kuze, J.-Y. Son, Y.-T. Cui, H. Oji, S. Komaba, *ChemElectroChem* **2014**, 1, 580.
- [50] M. Mayo, K. J. Griffith, C. J. Pickard, A. J. Morris, *Chem. Mater.* **2016**, 28, 2011.
- [51] a) J. M. Sangster, *J. Phase Equilib. Diffus.* **2009**, 31, 62; b) R. Morita, K. Gotoh, M. Dahbi, K. Kubota, S. Komaba, K. Tokiwa, S. Arabnejad, K. Yamashita, K. Deguchi, S. Ohki, T. Shimizu, R. Laskowski, H. Ishida, *J. Power Sources* **2019**, 413, 418.
- [52] L. E. Marbella, M. L. Evans, M. F. Groh, J. Nelson, K. J. Griffith, A. J. Morris, C. P. Grey, *J. Am. Chem. Soc.* **2018**, 140, 7994.
- [53] S. Kaushik, K. Matsumoto, Y. Oriksa, M. Katayama, Y. Inada, Y. Sato, K. Gotoh, H. Ando, R. Hagiwara, *J. Power Sources* **2021**, 483, 229182.
- [54] G. Coquil, B. Fraisse, N. Dupré, L. Monconduit, *ACS Appl. Mater. Interfaces* **2018**, 1, 3778.
- [55] M. A. Hope, A. C. Forse, K. J. Griffith, M. R. Lukatskaya, M. Ghidiu, Y. Gogotsi, C. P. Grey, *Phys. Chem. Chem. Phys.* **2016**, 18, 5099.
- [56] S. Kajiyama, L. Szabova, K. Sodeyama, H. Iinuma, R. Morita, K. Gotoh, Y. Tateyama, M. Okubo, A. Yamada, *ACS Nano* **2016**, 10, 3334–3341.
- [57] M. Zarrabeitia, E. Castillo-Martinez, J. M. López Del Amo, A. Eguia-Barrio, M. A. Muñoz-Márquez, T. Rojo, M. Casas-Cabanas, *J. Power Sources* **2016**, 324, 378.

Manuscript received: November 30, 2020

Revised manuscript received: February 6, 2021

Accepted manuscript online: February 8, 2021

Version of record online: March 4, 2021